

SAMI3 simulations of ionospheric metallic layers at Arecibo

J. Krall¹, J. D. Huba², E. Noss³ and D. P. Drob⁴

¹Plasma Physics Division, Naval Research Laboratory, Washington, District of Columbia, USA

²Syntek Technologies, Fairfax, VA, USA

³National Research Council Postdoctoral Research Associate, Plasma Physics Division, Naval Research Laboratory,
Washington, District of Columbia, USA

⁴Space Science Division, Naval Research Laboratory, Washington, District of Columbia, USA

Key Points:

- SAMI3 describes metallic layers observed at Arecibo.
- Layers supported by zonal and meridional wind shear and electric fields.
- Metallic layers below 110 km associated mainly with meridional wind shear.

Corresponding author: Jonathan Krall, jonathan.krall@nrl.navy.mil

Abstract

The Naval Research Laboratory (NRL) Sami3 is Also a Model of the Ionosphere (SAMI3) ionosphere/plasmasphere code is used to examine the physics of metallic layers at altitudes from 80 to 160 km. Results are presented near the simulated location of the Arecibo observatory (18N, 66W). We find that simulations, using winds from the empirical horizontal wind model (HWM14), produce layers consistent with those observed at Arecibo. Specifically, we find upper semidiurnal and lower diurnal traces similar to those identified in previous observational surveys. While metallic layers are shaped by meridional winds, zonal winds, and electric fields, much of the observed structure is found if only meridional wind forces are included in the model. Stratification below 110 km, where the ions are very weakly magnetized, is supported mainly by meridional wind shear.

1 Introduction

As a result of meteor ablation, Earth’s atmosphere includes a variety of metal components. These are of interest because remote measurements of metal atoms provide useful diagnostics of wind speed and temperature [Chu and Yu, 2017] and because metal ion layers can affect the propagation of electromagnetic waves through the ionosphere. These can appear in ionosondes as localized density peaks in the ionosphere *E* region; they are known as ‘sporadic *E* layers’ [Young *et al.*, 1967]. Despite their name, observations show that sporadic *E* layers occur almost daily [Mathews, 1998]. Because sporadic *E* layers can interfere with communication and navigation signals, they are the focus of our present work.

High-density layers of metallic ions occur where converging vertical ion drifts cause ions to collect, increasing their density [e.g. Haldoupis, 2011]. These can be driven by zonal [Whitehead, 1961] or meridional [Axford, 1963] winds. Axford [1963] specifically addresses the direct effect of meridional winds acting on magnetized or partially-magnetized ions. Meridional wind shear versus height can lead to layer formation, as long as the magnetic field is neither exactly horizontal (equator) nor exactly vertical (poles). MacLeod [1966] described several wind-driven stratification mechanisms, including the wind-driven $\mathbf{U} \times \mathbf{B}$ drifts of Whitehead [1961]. Here, \mathbf{U} is the wind and \mathbf{B} is the geomagnetic field. These occur where the ions are both partially magnetized (so ions gyrate about \mathbf{B}) and partially collisional (so the wind can affect the gyro motion). MacLeod [1966] notes that, because collisionality affects the vertical drift speed and varies with height, converging vertical drifts can occur even when meridional or zonal winds are constant versus height. Later, Nygrén *et al.* [1984] showed that a vertical shear in the $\mathbf{E} \times \mathbf{B}$ drift can also cause stratification, particularly at high latitudes.

In the present study, we use the SAMI3 (Sami3 is also a model of the ionosphere) model to explore these stratification mechanisms and to demonstrate that the present modeling effort reproduces observed features of metallic *E* region layers. We will specifically focus on layers observed at the Arecibo Observatory (latitude 18°N, longitude 66°W), such as those reported by Christakis *et al.* [2009]. The SAMI3 code was recently updated to include metallic ions (Mg^+ and Fe^+) and *E* region collisional transport [Huba *et al.*, 2019]. What is new in the present work is the simulation of wind-driven and $\mathbf{E} \times \mathbf{B}$ -driven stratification in the context of a global model of the ionosphere.

Previous global modeling of metallic ions, particularly using the WACCM (whole atmosphere community climate model), did not include wind-driven transport of the metallic ion species [Feng *et al.*, 2013]. These mechanisms have been simulated by others, however. Using a 1D version of their 2D model, Carter and Forbes [1999, Fig. 4] show that meridional winds, zonal winds, and $\mathbf{E} \times \mathbf{B}$ drifts each contribute significantly to vertical ion drifts. More specifically, they find meridional winds dominate at altitudes above 130 km, with zonal winds having increased influence below 130 km. Chu and Yu [2017] simulated these same mechanisms at high latitudes, also including the vertical winds that

are one component of gravity waves. In the present study, we will not include such local waves. We instead consider stratification driven by ever-present atmospheric tides.

We proceed as follows. We begin with a discussion of observed stratification at Arecibo. Here we show incoherent scatter data that illustrates typical *E* region stratification. This is followed by a brief discussion of the SAMI3 code and the simulation conditions. Rather than simulate a specific event, we use typical atmosphere conditions, with winds computed using the empirical Horizontal Wind Model (HWM14) [Drob *et al.*, 2015]. We will show that many of the observed features are obtained in our results and that individual layers correspond to converging zero-crossings in the vertical drift profile. While we will see that layers generally correspond to features in the meridional or zonal wind profiles, the correspondence is not always clear. In this analysis, we will see that a descending layer can remain coherent even as it descends from a highly-magnetized altitude to a lower, more collisional regime. Here, we will illustrate the heights at which zonal (roughly 110 km to 130 km) and meridional (other heights) wind effects seem to dominate the stratification. This is followed by a discussion of day-to-day variability in the observed layers and corresponding features in the simulations.

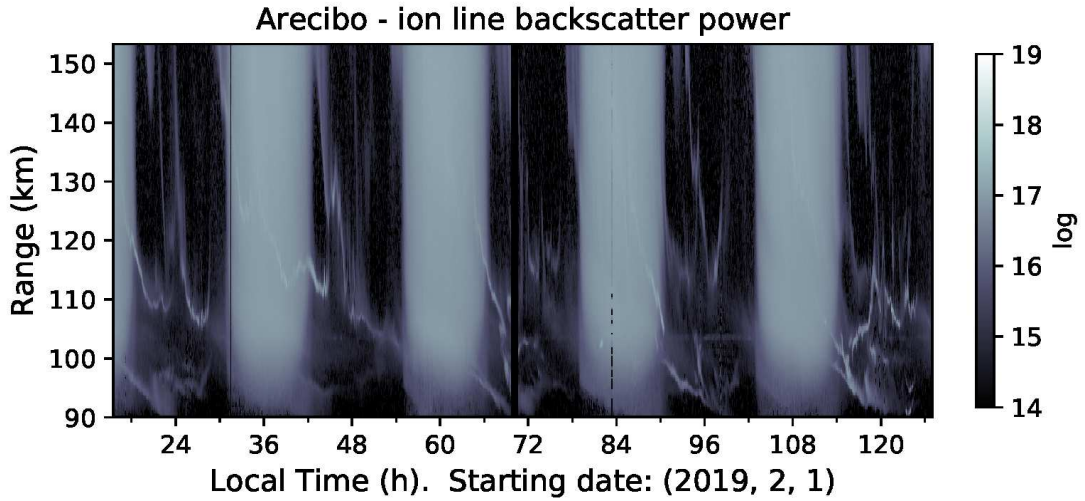


Figure 1. Arecibo ion line uncalibrated range-time-intensity plot from the 430 MHz incoherent scatter radar (ISR) during a World Day period from 11:36 UT 1 February to 02:48 UT 6 February 2019. Here the plot range is almost equivalent to height; the data was collected using the Gregorian feed system pointing 1.06 degrees from zenith with no azimuth swinging. The ISR was operated alternating 10 s of topside mode and 50 s of a pseudorandom-coded long pulse (CLP) [Sulzer, 1986]. The data shown here corresponds exclusively to the CLP mode with 10 ms inter-pulse-period (IPP), 440 μ s of pulse-length. It is processed with 2 μ s bauds to obtain a range resolution of 300 m. The approximate cadence is five profiles per two minutes.

2 Layers observed at Arecibo

So-called sporadic *E* layers occur almost daily at Arecibo [Mathews, 1998]. The observed dependence of these layers on tides [Mathews and Bekeny, 1979; Pancheva *et al.*, 2003] is strong enough that they are sometimes called tidal ion layers [Mathews, 1998]. In a study of 140 days of Arecibo radar data, distributed over many years and all seasons, Christakis *et al.* [2009] identifies three commonly-observed layers, the upper semidiurnal day and night layers and the lower diurnal layer. While these data show significant day-to-

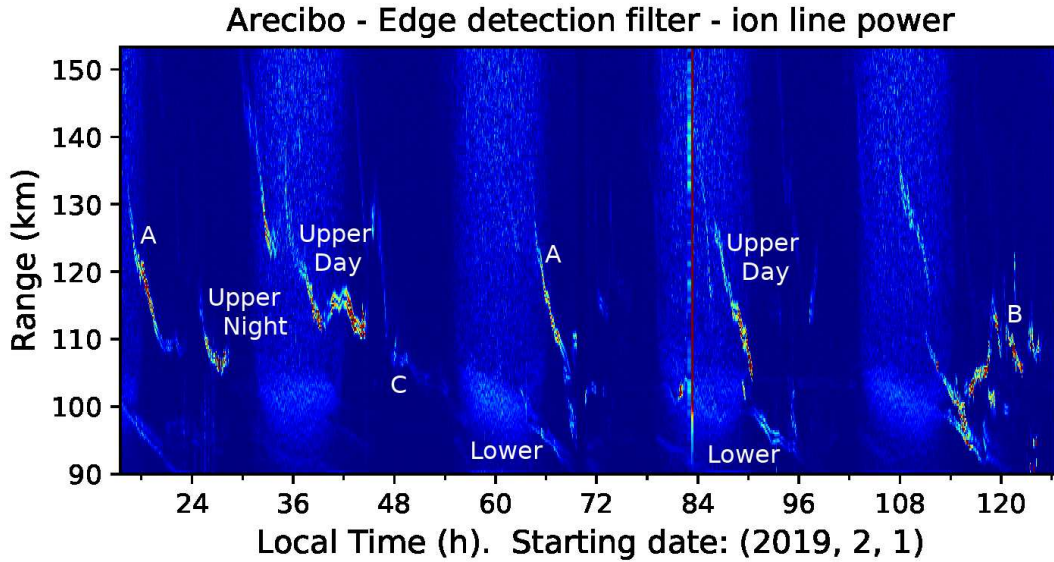


Figure 2. Arecibo data from Figure 1 filtered to highlight edges. A Sobel gradient operator was applied to the ion line data to detect the boundaries of the descendent layers, which are difficult to observe during the day due to high ionization rates. Upper semidiurnal day layers are identified at hours 34-46 and 86-92 (local time beginning 00:00 LT 1 February). An upper semidiurnal night layer is observed at hours 25-29. A lower diurnal layer appears almost daily; two of these are labeled. Features A, B, and C are discussed in the text.

day variability, the three types of layers are observed throughout the year [Christakis *et al.*, 2009, Fig. 8].

An example of these layers can be seen in Figure 1, which shows a range-time-intensity plot of the ion-line signal recorded at Arecibo from 11:36 UT 1 February to 02:48 UT 6 February 2019. The ion line is produced by the modified Thomson scatter from thermal fluctuations associated with ion acoustic waves [Evans, 1969]. The backscatter is very weak and requires large radars to be detected. The Gregorian feed system of the Arecibo 430 MHz radar uses $\sim 70\%$ of the 350-m reflector dish [Isham *et al.*, 2000] to obtain a gain of the order of 61 dB. That allows detection of the small radar cross-section of the charged particles present in the ionosphere, as shown in Figure 1. However, the strong diurnal background ionization can mask the backscatter from the descending layers. To highlight the layers, we applied an edge-enhancing gradient-operator Sobel-filter to the data shown in Figure 1. The edge detection algorithm finds the high-intensity variations in the vertical and horizontal direction; the result is shown in Figure 2.

Visible in Figure 2 are upper semidiurnal day layers ('Upper Day'), generally resembling the Christakis *et al.* [2009] description. Upper layers near hour 18 and hour 66, labeled 'A,' descending from 130 to 110 km during local time 16:00 to 22:00, appear to be upper semidiurnal day layers, shifted by about 6 hours to later local times. An upper semidiurnal night layer ('Upper Night') is visible from hours 25-29. An upper layer near hour 120 ('B'), is similar to the semidiurnal nighttime layer of Christakis *et al.* [2009], but is less coherent than the example at hours 25-29.

The lower diurnal layer appears almost daily. It is most visible during the local night but also present during the day, descending from above 100 km (during the day) to about 90 km (around midnight). The Christakis *et al.* [2009] description leads us to expect that these begin at height 105 km during local daytime, but there are only hints in these data that the lower layer is present during each day before becoming more visible at night. In

one case, labeled ‘C,’ a weak lower layer seems to form about 1 hour before midnight and descend continuously through the day and into the next night, fading at about 22:00 LT (hour 70 in Figure 2). However, further analysis shows a break between feature C and the lower layer at 07:45 LT. This suggests that they are two different layers. While the lower layer is not visible during the day, additional analysis shows that this relatively weak layer is present while being nearly overwhelmed by the background *E* layer. Beginning at 08:30 LT and altitude 107 km, it slowly descends until about 22:00 LT (hours 56.5-70 in Figure 2).

3 Modeling

To describe the system we use the SAMI3 ionosphere/plasmasphere code [Huba *et al.*, 2005; Huba and Krall, 2013], which has been recently modified to include metallic ions Fe^+ and Mg^+ [Huba *et al.*, 2019]. SAMI3 is based on the SAMI2 (Sami2 is Another Model of the Ionosphere) code [Huba *et al.*, 2000a]. The SAMI3 grid is arranged with one axis parallel to the geomagnetic field. For these runs we used 248 ‘field lines,’ 404 grid points along each field line, and 96 longitudes. Ion motion parallel to the field is governed by the momentum equation. Ion motion perpendicular to the magnetic field is governed by drift equations presented in Huba *et al.* [2019]. Here, perpendicular drifts include terms corresponding to collisional forces exerted by the background wind. The inclusion of these drifts allows the SAMI3 model to describe transport in the ionosphere *E* layer and below.

SAMI3 solves plasma transport and electric potential equations numerically versus time. To simplify the analysis of the simulations presented here, the model magnetic field is approximated to be a dipole that rotates with Earth. We have also performed simulations with the Apex Model [Richmond and Kamide, 1988] being used to compute the magnetic coordinate grid. Winds are computed using the HWM14 empirical model [Drob *et al.*, 2015]. HWM14 winds vary with time of year but do not exhibit day-to-day variability during geomagnetically quiet conditions. Atmospheric composition is computed using the NRLMSISE-00 [Picone *et al.*, 2002] version of the MSIS (mass spectrometer and incoherent scatter) empirical atmosphere model.

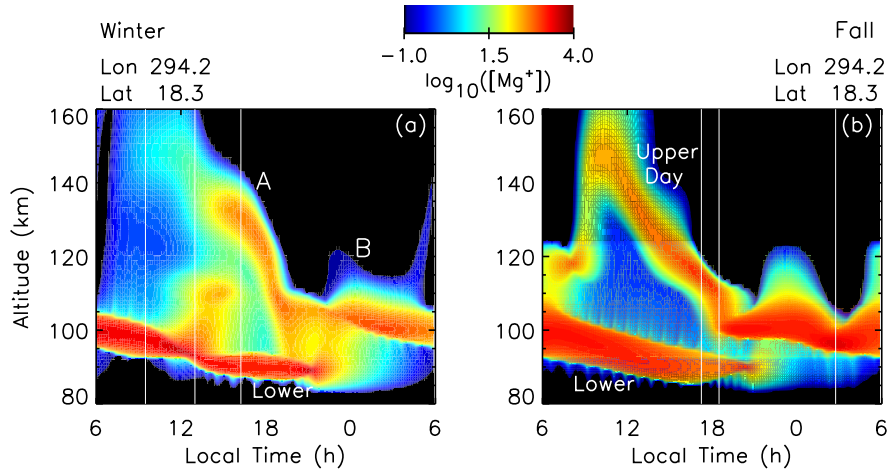


Figure 3. SAMI3 layers at the Arecibo geographic coordinates. Plotted is the logarithm of the Mg^+ density (cm^{-3}) versus local time and altitude along a field line that passes above Arecibo. Plots are representative of (a) winter, 20 January, and (b) fall, 20 October, conditions.

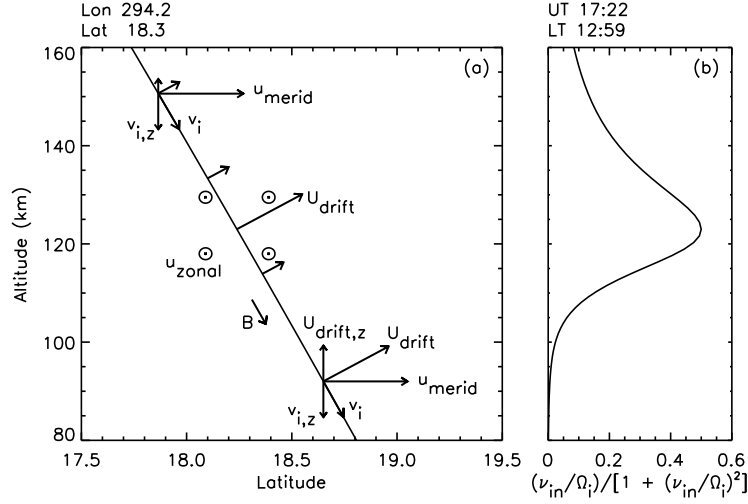


Figure 4. (a) A field line is plotted, along with example meridional (positive northward) and zonal (positive out of the page) wind vectors. Resulting field-aligned (v_i) and perpendicular (U_{drift}) motions are indicated. (b) $\alpha_1 = (\nu_{in}/\Omega_i)/[1 + (\nu_{in}/\Omega_i)^2]$ versus altitude for the simulation of Figure 3(a).

4 Results

We performed SAMI3 simulations for winter conditions, similar to those of Figure 2. Each 36-hour simulation begins with a uniform Mg^+ layer at altitude 105 km, with density 10^3 cm^{-3} and a half width of 5 km. Because the current HWM14 wind model does not have the day-to-day variability suggested in the data, we simulated four different seasons of the year, two of which are shown in Figure 3. A variety of descending layers can be seen in Figure 3, where the logarithm of the Mg^+ density is plotted versus height and local time along a field line that passes through latitude 18.3° and altitude 120 km.

As in Figure 2, the upper semidiurnal day layer appears in Figure 3b. In Figure 3a, this layer seems to be shifted by 2-3 hours. Like the similar layer near hour 66 in the data (also apparently an upper semidiurnal day layer shifted in local time), it is labeled A. Similar to most nights in Figure 2, the upper semidiurnal night layer isn't clearly visible. A weak feature at the correct altitude and local time is labeled B in Figure 3a. Also similar to Figure 2, lower diurnal layers descend from 105 km to 90 km on each day of Figure 3. However, whereas *Christakis et al.* [2009] reports these to begin at 06:00 LT and end after 24:00 LT, the lower layers in Figure 3 begin at about 00:00 LT and end about 3 hours before 24:00 LT; relative to the reported data, they are shifted by 3-6 hours.

We now consider the mechanisms that drive stratification at these heights under the approximation of zero vertical winds. Figure 4a shows how winds (u_{merid} and u_{zonal}) drive ion motions parallel (v_i) and perpendicular (U_{drift}) to \mathbf{B} . Plotted is a field line in the northern hemisphere, along with representative wind and drift vectors. Neglecting ion gravity, pressure gradients, and ion-ion collisions, the governing equation for parallel ion motion is [Huba *et al.*, 2000b],

$$\frac{\partial v_i}{\partial t} + \mathbf{v}_i \cdot \nabla \mathbf{v}_i = -\nu_{in}(\mathbf{v}_i - u_{\parallel}), \quad (1)$$

where \mathbf{v}_i is the ion velocity, v_i is the component of ion velocity parallel to \mathbf{B} , ν_{in} is the ion-neutral collision frequency, and u_{\parallel} is the component of the wind parallel to \mathbf{B} . The drift equation for perpendicular ion motion, which neglects ion inertia, is [Huba *et al.*,

2019]

$$\mathbf{U}_{\text{drift}} = \alpha_0 \frac{c\mathbf{E}_\perp}{B} \times \hat{\mathbf{e}}_b + \alpha_1 (\mathbf{u}_\perp \times \hat{\mathbf{e}}_b + \frac{c\mathbf{E}_\perp}{B}) + \alpha_2 \mathbf{u}_\perp \quad (2)$$

where E_\perp and u_\perp are the electric field and wind components perpendicular to $\mathbf{B} = B\hat{\mathbf{e}}_b$. The collisional factors in equation (2) are $\alpha_0 = 1/[1 + (v_{in}/\Omega_i)^2]$, $\alpha_1 = \alpha_0(v_{in}/\Omega_i)$, and $\alpha_2 = \alpha_0(v_{in}/\Omega_i)^2$, where Ω_i is the ion gyrofrequency. For simplicity, the gravity term is not shown in equation (2).

Zonal winds, directed out of the plane of the image in Figure 4a, drive $\mathbf{u} \times \mathbf{B}$ drifts via the second term in equation (2). The $\mathbf{u} \times \mathbf{B}$ drift is proportional to $\alpha_1 = (v_{in}/\Omega_i)/[1 + (v_{in}/\Omega_i)^2]$ and occurs only when ions are both sufficiently magnetized, to provide a gyro motion, and sufficiently collisional, to provide a force that affects gyro orbits. They peak when $v_{in} = \Omega_i$. Figure 4b shows a typical profile of α_1 versus altitude, indicating the transition from an unmagnetized ionosphere at low altitude to a magnetized ionosphere at high altitude. Returning to Figure 4a, a constant zonal wind field, indicated by vectors directed out of the page, causes a peak $\mathbf{u} \times \mathbf{B}$ drift at altitude 123 km. Above and below this altitude, the drift speed falls with the α_1 factor.

At high altitude, where the ions are nearly fully magnetized, a northward horizontal meridional wind causes a net downward ion motion. This is illustrated schematically in the upper left of Figure 4a. At low altitude, where the ions are collisional, a northward meridional wind leads mainly to a corresponding horizontal ion velocity, $\mathbf{v}_i \simeq \mathbf{u}_{\text{merid}}$, and the net vertical ion motion is close to zero. This is illustrated in the lower right of Figure 4a, where the z component of the drift $U_{\text{drift},z}$ is almost exactly equal and opposite to z component of the field-aligned ion motion $v_{i,z}$. Because the magnetic field still has an influence at these altitudes, $U_{\text{drift},z}$ does not exactly cancel out $v_{i,z}$, and stratification can be supported by wind shear.

Results from Figure 3a are analyzed in terms of the simulated ion motions in Figure 5. The left-hand panels, Figure 5(a,d,g), show vertical profiles of the Mg^+ density at three different times. The three time-values in Figure 5 are marked by vertical lines in Figure 3a. The center panels, Figure 5(b,e,h), show corresponding vertical profiles of the vertical component of the field-aligned Mg^+ velocity, $v_{i,z}$, and the perpendicular drift velocity, $U_{\text{drift},z}$. Where the net vertical motion (solid curve in Figure 5b) is converging, marked arrows in Figure 5(a,b), a layer can develop.

The right-hand panels, Figure 5(c,f,i) show profiles of the meridional (u_{merid}) and zonal (u_{zonal}) winds. As noted in Figure 4, the meridional wind can directly push ions along the field line with a northward (positive) wind causing a downward ion motion. For this reason the z -component of the field-aligned motion ($v_{i,z}$, dashed curve) in Figure 5b approximately mirrors the meridional wind (u_{merid} , dashed curve) in Figure 5c. More to the point, the convergence point in $v_{i,z}(z) + U_{\text{drift},z}$ in Figure 5b corresponds to a shear in $u_{\text{merid}}(z)$ in Figure 5c.

Over time, the convergence point, marked by an arrow at 12:59 LT in Figure 5e and at 16:14 LT in Figure 5h, descends. The layer descends with it. At 12:59 LT, Figure 5d, the layer is at altitude 140 km and the shear in $v_{i,z}(z) + U_{\text{drift},z}$ corresponds only to a vertical gradient in $(v_{in}/\Omega_i)/[1 + (v_{in}/\Omega_i)^2]$ (Figure 4b) and a corresponding shear in $U_{\text{drift},z}$ (Figure 5e, long-dashed lines). At this time and at altitude 140 km, winds are approximately constant versus z . At 16:14 LT, Figure 5g, the layer is at altitude 130 km, where $v_{in} \simeq \Omega_i$ and vertical velocities from zonal winds relatively large. Here, the shear in $v_{i,z}(z) + U_{\text{drift},z}$, Figure 5h (solid curve), corresponds to a shear in the zonal wind speed, Figure 5i (long-dashed curve).

As shown in Figure 4a above, at low altitude the vertical components of parallel and perpendicular ion motions associated with the meridional wind tend to cancel out (lower right of figure). This can be seen at altitudes below 100 km in Figure 5(b,e,h), where the

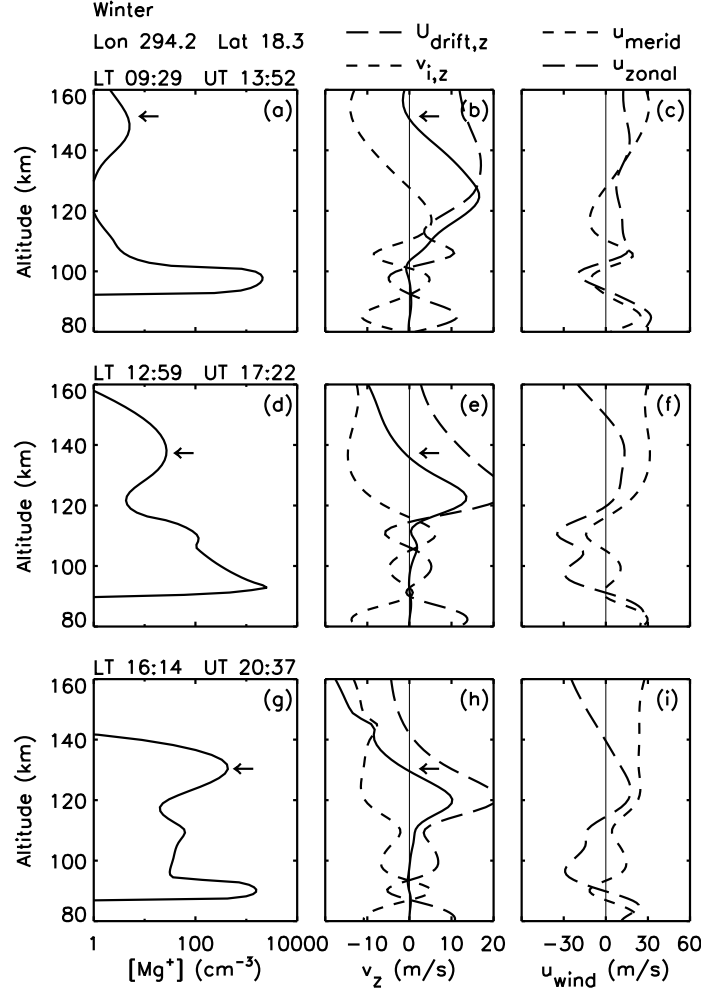


Figure 5. (a,d,g) Mg^+ density plotted versus height along a field line at three different times for the winter simulation of Figure 3a. (b,e,h) The vertical component of ion motion parallel ($v_{i,z}$, dash), and perpendicular ($U_{\text{drift},z}$, long dash) to the field line is plotted along with the net vertical motion (solid). (c,f,i) Meridional (dash) and zonal (long dash) winds.

dashed lines ($v_{i,z}$) are approximately equal and opposite to the long-dashed lines ($U_{\text{drift},z}$) and the net vertical motion (solid line) is very small.

Low-altitude dynamics are shown in Figure 6. Here we repeat the format of Figure 5 except in Figure 6(b,e,h), where only the net vertical motion, $v_{i,z} + U_{\text{drift},z}$, is shown and only a narrow range of velocities is included. Above 120 km, $v_{i,z} + U_{\text{drift},z}$ is generally too large to be seen in the plot. The three time-values in Figure 6 are marked by vertical lines in Figure 3b. At 17:14 LT, Figure 6a, two layers are evident (labeled A,C), corresponding to convergence points above two local peaks (A,C) in $v_{i,z} + U_{\text{drift},z}$, Figure 6b. At 18:29 LT, Figure 6d, layer A is no longer supported and a new layer B is emerging. The new layer corresponds to a convergence point above peak B in the vertical motion, Figure 6e. At this time, layer C is still present. At 02:44 LT, Figure 6g, layer C is no longer supported and layers A and C have faded away. Layer B remains, having descended slowly during the intervening 8 hours. At 17:14 LT, the convergence point supporting layer A

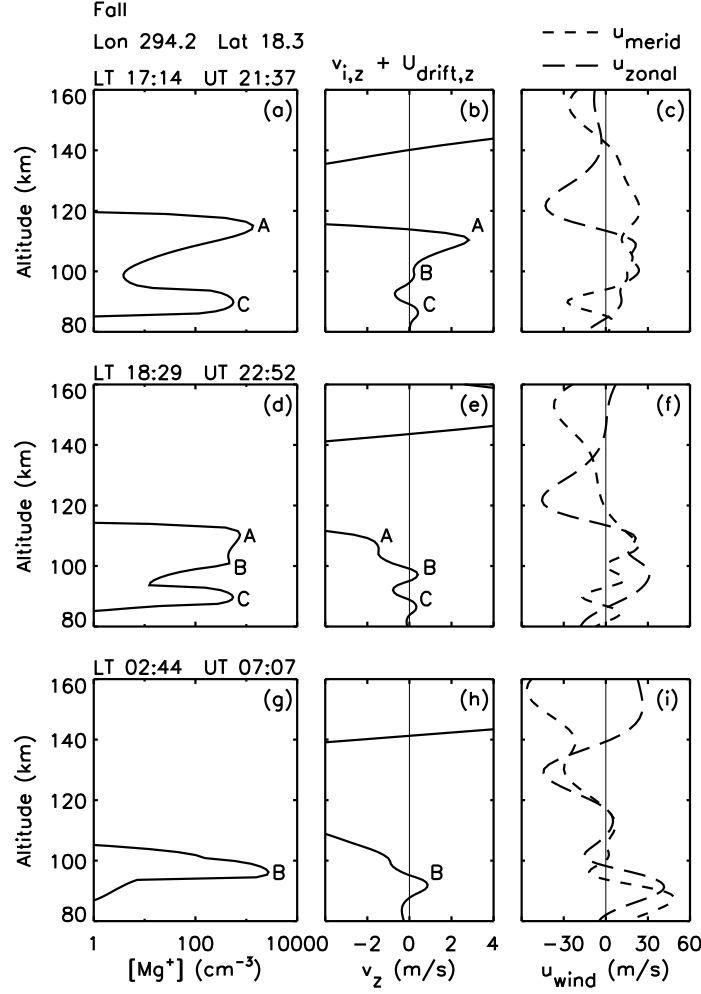


Figure 6. (a,d,g) Mg^+ density plotted versus height along a field line at three different times for the fall simulation of Figure 3b. (b,e,h) Net vertical ion motion, $v_{i,z} + U_{\text{drift},z}$. (c,f,i) Meridional (dash) and zonal (long dash) winds.

appears to correspond to a vertical shear in the zonal wind, Figure 6c (long-dash curve). In all other cases, the correspondence between the net vertical velocity, Figure 6(b,e,h), and the wind profiles, Figure 6(c,f,i), is unclear. Below we will revisit low altitude layers, focusing on the role of the meridional wind.

We now focus on the direct effects of individual wind components (zonal or meridional) acting on these metal ion layers as shown in Figure 4. Figure 7a shows the winter simulation of Figure 3a, but with only the direct zonal wind effects included; no meridional winds and no wind-driven \mathbf{E} fields. Similarly, Figure 7b, includes only the direct meridional wind effects.

Figures 7a and 7b are quite different from Figure 3a. The exception is the lower portion of Figure 7b, which, at altitudes below 110km, is remarkably similar to Figure 3a. Figure 7 shows that either zonal or meridional winds can shape layers. Consistent with Figure 5, where the upper semidiurnal day layer was shown to be supported by a combination of meridional and zonal winds, neither wind component dominates at all altitudes

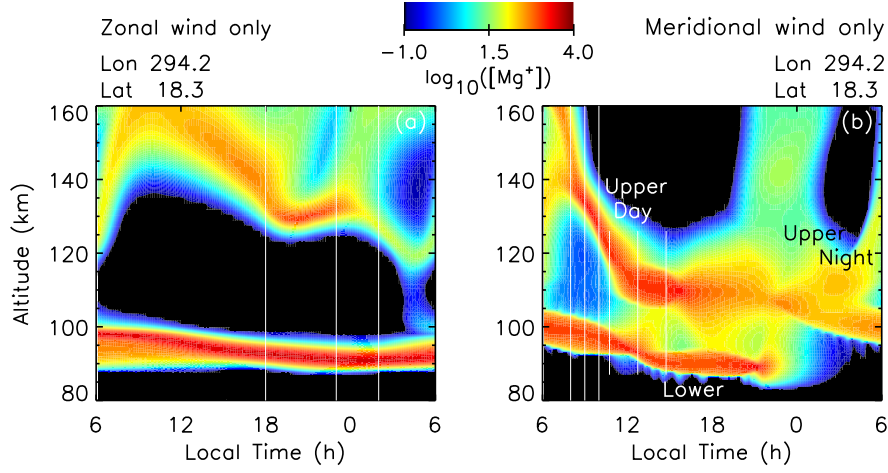


Figure 7. Same as Figure 3a but with (a) zonal winds only and (b) meridional winds only. Wind-driven \mathbf{E} fields are excluded.

above 110 km. However, Figure 7b suggests that meridional winds are the main driver of stratification below 110 km. Figure 7 also shows that either zonal or meridional winds, acting alone, can transport metal ions upwards from altitude 105 km, where Mg^+ ions were initially located.

The example of Figure 7a is analyzed in Figure 8 at times marked by vertical lines in Figure 7a. At 17:59 LT, a thick Mg^+ layer, Figure 8a, marked with an arrow, is supported by a converging shear in the vertical ion velocity $U_{\text{drift},z}$, Figure 8b, corresponding to a shear in the zonal wind Figure 8c. At 22:59 LT, the Mg^+ layer, Figure 8d, is no longer fully supported. The zonal wind shear is still present, Figure 8f, but does not produce a converging vertical ion velocity profile with a zero crossing, Figure 8e. This situation, where the layer is not fully supported, lasts three hours. At 01:59 LT the Mg^+ layer is once again supported, but weaker, Figure 8g. Additional analysis shows that the lower layer in Figure 7a is not always supported by wind shear. At those times the Mg^+ ions fall to about 90 km altitude and are slowly lost to recombination. Below altitude 100 km, vertical motions driven by zonal winds are very small, with $|U_{\text{drift},z} + v_{i,z}| < 0.6$ m/s at all times.

Figure 7b suggests that meridional winds alone can produce, more or less, all three of the traces identified by *Christakis et al.* [2009]: the upper day and night semidiurnal layers and the lower diurnal layer. These are labeled in Figure 7b. However, we emphasize that actual stratification at altitudes above 110 km is influenced by a combination of zonal winds, meridional winds, and $\mathbf{E} \times \mathbf{B}$ drifts. Figure 9 shows that meridional wind-driven ion velocities parallel to \mathbf{B} can explain the stratification in Figure 7b. Specifically, arrows in Figure 9 highlight the upper semidiurnal day layer at local times 07:59, 08:59 and 09:59; these times are marked by long vertical lines in Figure 7b. As in Figure 5, $v_{i,z}$, dashed lines in Figure 9(b,e,h), roughly mirror the meridional winds, Figure 9(c,f,i).

Further analysis of this case, shown in Figure 10, verifies that the lower layer corresponds to a zero-crossing in the net vertical ion motion. As in Figure 6(b,e,h), only a narrow range of velocities is included in the center column (panels b,e,h). Arrows in Figure 10 highlight the lower layer of Figure 7b at local times 10:44, 12:44, and 14:44; these times are marked with short vertical lines in Figure 7b. In the highly-collisional regime below 110 km, we expect $\mathbf{v}_i \approx \mathbf{u}$ and, as shown in Figure 4a, $U_{\text{drift},z} \approx -v_{i,z}$. However, we find a small net vertical wind-driven motion, generally with $U_{\text{drift},z} > -v_{i,z}$ and with $v_{i,z}$ and $U_{\text{drift},z}$ being slightly out of phase. This can be seen in Figure 10b, where $v_{i,z}$

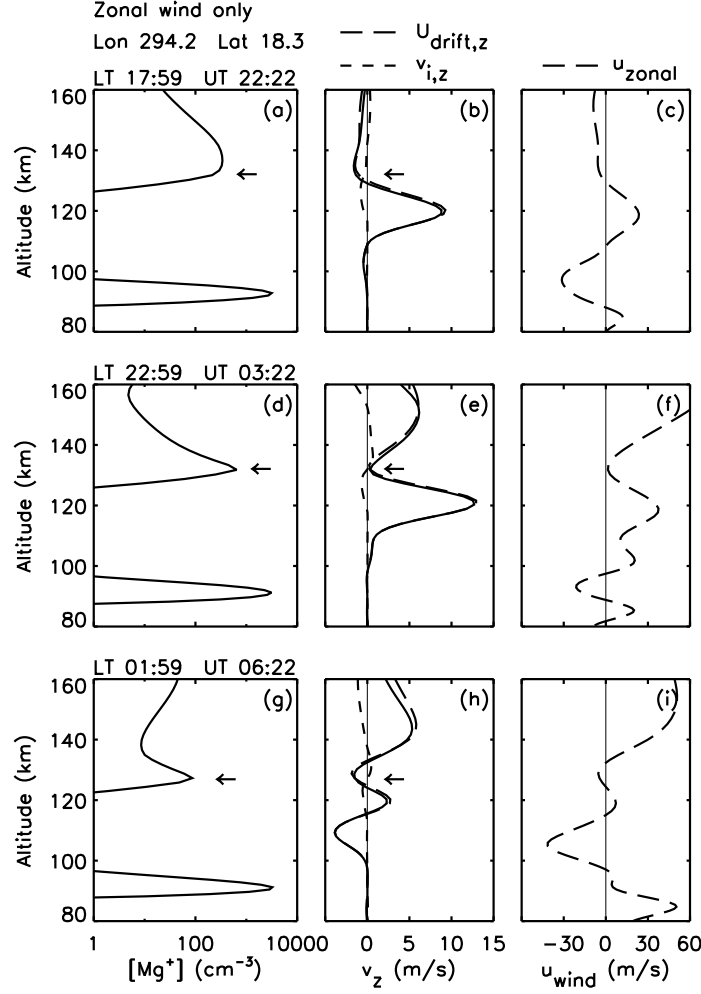


Figure 8. Similar to Figure 5, but with only direct zonal wind effects (no wind-driven \mathbf{E} fields).

(dashed curve) and $U_{\text{drift},z}$ (long dash curve) are also shown. Wind-driven vertical motions are again small, though not as small as in the zonal-wind-only case. Here, for altitudes less than 100 km, $|U_{\text{drift},z} + v_{i,z}| < 1.5$ m/s at all times.

5 Discussion

The simulated layers of Figure 3 compare well to the actual layers of Figure 2 and to others reported at Arecibo [Christakis *et al.*, 2009]. Of the three features identified in the extensive study by Christakis *et al.* [2009], two (upper semidiurnal day and lower diurnal layers) are easily found in our example data and in our simulations. The third, the upper semidiurnal night layer, clearly occurs only in the data. It is only hinted at in our modeling (Figure 3a, feature B and Figure 7b).

In Figures 2 and 3a above, we identify an upper layer as ‘feature A.’ Our hypothesis is that this is an upper semidiurnal day layer shifted about 6 hours later in local time relative to the corresponding layer in Christakis *et al.* [2009, Fig. 8]. Supported by a combination of zonal winds, meridional winds, and $\mathbf{E} \times \mathbf{B}$ drifts, we see that the upper semi-

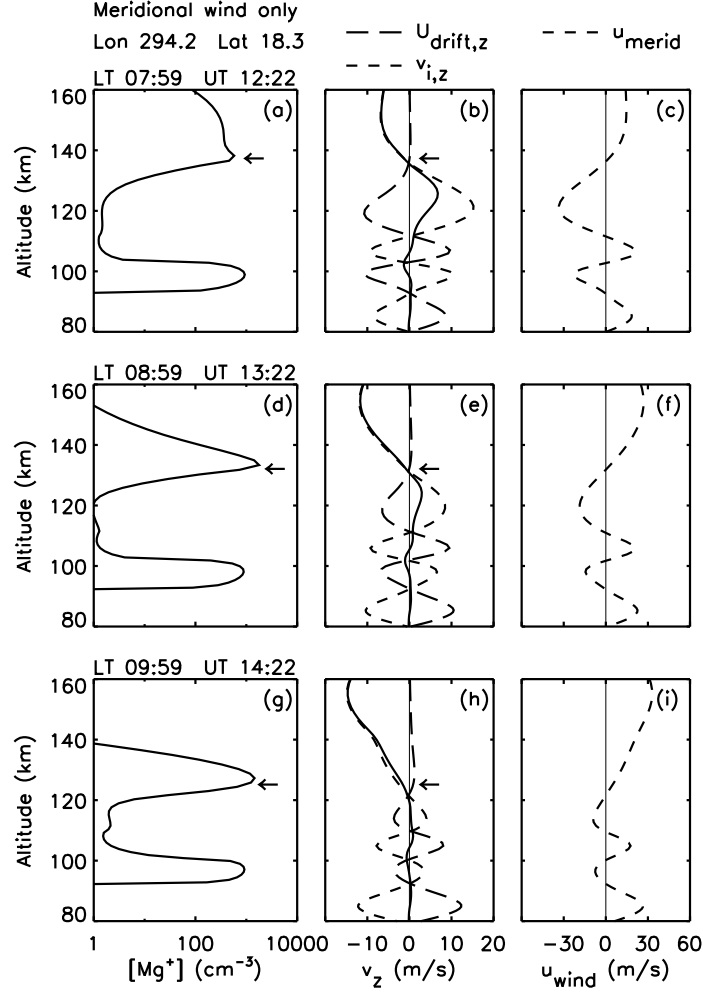


Figure 9. Similar to Figure 5, but with only meridional winds.

urnal day layer tends to shift in local time from day to day. In fact, if the zonal winds are excluded entirely, this layer (Figure 3, feature A) is still present but shifted to earlier local times (Figure 7b).

The lower diurnal layer is clearly present in four out of the five days shown in Figure 2 and in both days of Figure 3. In the simulations, the lower layer tends to fade before local midnight. This is in contrast to *Christakis et al.* [2009, Fig. 8], where the lower diurnal layer persists for 2-5 hours past local midnight. Two examples of lower layers are labeled in Figure 2. One, hours 56-69, fades out before local midnight, similar to the model examples. Another, hours 87-99, persists past local midnight, as in the *Christakis et al.* [2009, Fig. 8] description.

In summary, we are able to identify the upper day and night semidiurnal layers as and the lower diurnal layer in both data and simulations. However, these are often shifted by up to 6 hours in local time relative to the statistical average, as presented by *Christakis et al.* [2009]. In fact, day-to-day phase shifts of up to 6 hours are common for both the diurnal and semidiurnal atmospheric tides. This day-to-day variability is not captured in the HWM14 [*Drob et al.*, 2015] wind model used here. Because HWM14 does capture sea-

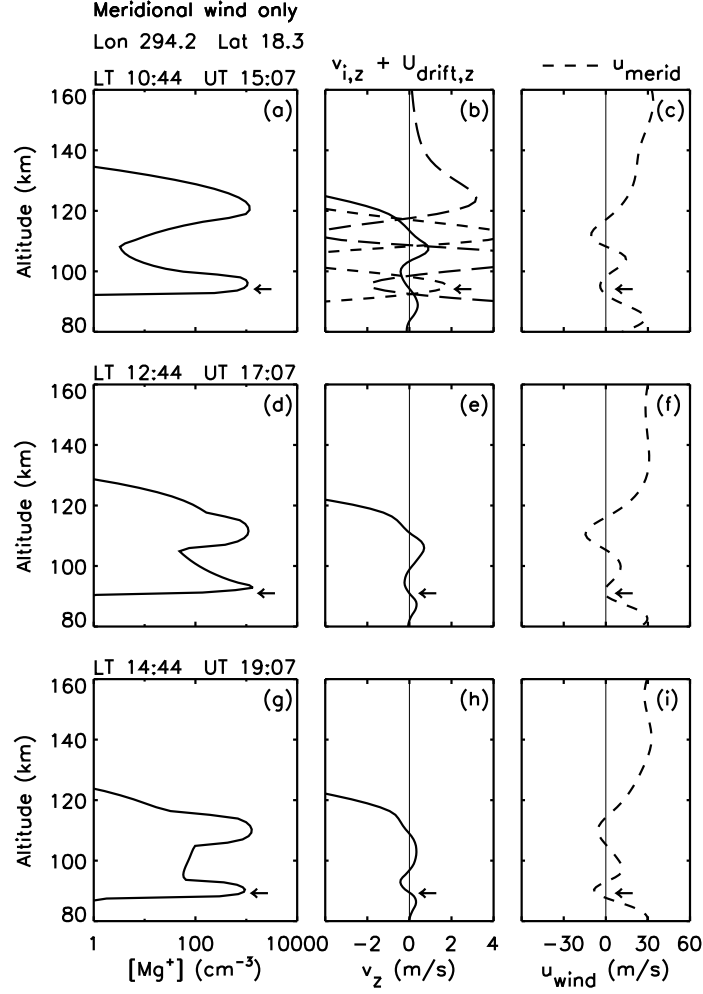


Figure 10. Similar to Figure 9, but at later times and with only the net vertical ion motion, $v_{i,z} + U_{\text{drift},z}$ shown in the center column. Arrows highlight the altitude of a zero-crossing in the net vertical motion that supports the lower layer. In panel (b) $v_{i,z}$ (dashed curve) and $U_{\text{drift},z}$ (long dash curve) are also shown.

sonal variations we obtained two different model days, in terms of the winds, by modeling two different seasons. In effect, we are using seasonal variability as a proxy for day-to-day variability. This is valid because the layers discussed here occur throughout the year.

We find that our simulations are consistent with past modeling. For example, in Figure 7, we find that meridional winds account for most of the stratification observed below 110 km, whereas stratification above 110 km is a mix of zonal, meridional, and $\mathbf{E} \times \mathbf{B}$ drifts. This might seem to contrast with *Carter and Forbes* [1999, Fig. 6], who suggest that meridional winds dominate at altitudes above 130 km, with zonal winds having increased influence below 130 km. To reconcile the two views, we note that, in Figure 5, we also see the transition from meridional control to zonal control of the layer as it descends to altitude 130 km. Consistent with theory [e.g. *Haldoupis*, 2011], both our modeling and that *Carter and Forbes* [1999] indicate a transition from meridional wind control to zonal wind control at about 130-140 km. However, the low-altitude < 110 km meridional-wind-driven stratification shown in Figures 7(b) and 9 is not found in ‘meridional winds only’

case shown by *Carter and Forbes* [1999, Fig. 6a]. While the model lower diurnal layer is consistent with observation, as expected, and is associated with wind shear, as expected, we find that it is associated with meridional rather than zonal winds. We reiterate that wind-driven net vertical velocities at altitudes below 100 km are rather small, of order 1 m/s. Factors not yet accounted for, such as vertical winds, might also be important in this regime.

Because the converging velocities that form layers above 110 km are driven by both meridional and zonal winds, the interplay between these two wind components might play a significant role. In future simulations, we plan to drive simulations using winds from a first-principles thermosphere code, such as TIMEGCM (Thermosphere Ionosphere Mesosphere Electrodynamics General Circulation Model) [Roble and Ridley, 1994; Crowley *et al.*, 1999] or GITM (Global Ionosphere-Thermosphere Model) [Ridley *et al.*, 2006], giving us zonal and meridional winds that are consistent with the fluid equations and with each other. The importance of self-consistency in the description of these layers, if any, is unknown.

In these simulations, we do not include additional deposition of metallic ions during the course of the simulation and do not model their atmospheric chemistry. The emphasis is on transport effects. For example, when we note that our model lower layers fade away at about 22:00 LT, we are saying that the ions are transported elsewhere. In their own modeling, *Carter and Forbes* [1999] found that stratification above 130 km was affected when the deposition was included. Nevertheless, we find that tidal winds and transport produce stratification consistent with observations.

6 Conclusion

Using SAMI3, we have simulated the global transport of an initially-uniform layer of Mg^+ and have analyzed results for comparison to *E* region stratification observed at Arecibo. While we clearly reproduce the upper semidiurnal day layer and the lower diurnal layer, these are often shifted by up to 6 hours in local time relative to the statistical average, as presented by *Christakis et al.* [2009]. The upper semidiurnal night layer is less prominent in the simulations (see Figure 3a, feature B, and Figure 7b).

We also present five days of incoherent scatter data (Figures 1 and 2), showing that the timing of these layers, especially the upper semidiurnal day layer, shows day-to-day phase shifts of up to 6 hours. We attribute these phase shifts to day-to-day variability in the diurnal and semidiurnal atmospheric tides. As in the simulations, the upper semidiurnal night layer is seen less often than the other two layers in these data. It occurs in only two of the five nights.

Consistent with prior modeling, especially that of *Carter and Forbes* [1999], we find a transition from meridional winds as the main driver of stratification above 135 km to zonal winds below 135 km. However, below 110 km, we find that meridional winds once again exert the dominant force.

Acknowledgments

This research was supported by NRL Base Funds and the NASA Heliophysics Supporting Research program. It was conducted while Eliana Nossa held a National Research Council Research Associateship at Naval Research Laboratory, Washington, DC. The Arecibo Observatory is a facility managed by UCF, YEL, and UMet under a cooperative agreement with the National Science Foundation. The authors thank Dr. Nestor Aponte, Dr. Mike Sulzer, and Phil Perillat for conducting the World Day observations at Arecibo Observatory. Arecibo World-Day data are available through the Madrigal database at <https://openmadrigal.org/>. Numerical data associated with each of the SAMI3 figures are

available from the publisher as supporting information for this publication. Current Horizontal Wind Model is available at <https://map.nrl.navy.mil/map/pub/nrl/HWM/HWM14/>.

References

- Axford, W. I. (1963), The formation and vertical movement of dense ionized layers in the ionosphere due to neutral wind shears, *Journal of Geophysical Research (1896-1977)*, 68(3), 769–779, doi:10.1029/JZ068i003p00769.
- Carter, L. N., and J. M. Forbes (1999), Global transport and localized layering of metallic ions in the upper atmosphere, *Annales Geophysicae*, 17(2), 190–209, doi:10.1007/s00585-999-0190-6.
- Christakis, N., C. Haldoupis, Q. Zhou, and C. Meek (2009), Seasonal variability and descent of mid-latitude sporadic E layers at Arecibo, *Annales Geophysicae*, 27(3), 923–931, doi:10.5194/angeo-27-923-2009.
- Chu, X., and Z. Yu (2017), Formation mechanisms of neutral Fe layers in the thermosphere at Antarctica studied with a thermosphere-ionosphere Fe/Fe⁺ (TIFe) model, *Journal of Geophysical Research: Space Physics*, 122(6), 6812–6848, doi:10.1002/2016JA023773.
- Crowley, G., C. Freitas, A. Ridley, D. Winningham, R. G. Roble, and A. D. Richmond (1999), Next generation space weather specification and forecasting model, Ionospheric Effects Symposium, Alexandria, Va.
- Drob, D. P., J. T. Emmert, J. W. Meriwether, J. J. Makela, E. Doornbos, M. Conde, G. Hernandez, J. Noto, K. A. Zawdie, S. E. McDonald, J. D. Huba, and J. H. Klenzing (2015), An update to the Horizontal Wind Model (HWM): The quiet time thermosphere, *Earth and Space Science*, 2(7), 301–319, doi:10.1002/2014EA000089.
- Evans, J. V. (1969), Theory and practice of ionosphere study by Thomson scatter radar, *Proceedings of the IEEE*, 57(4), 496–530, doi:10.1109/PROC.1969.7005.
- Feng, W., D. R. Marsh, M. P. Chipperfield, D. Janches, J. Höffner, F. Yi, and J. M. C. Plane (2013), A global atmospheric model of meteoric iron, *Journal of Geophysical Research: Atmospheres*, 118(16), 9456–9474, doi:10.1002/jgrd.50708.
- Haldoupis, C. (2011), *A Tutorial Review on Sporadic E Layers*, pp. 381–394, Springer Netherlands, Dordrecht, doi:10.1007/978-94-007-0326-1_29.
- Huba, J. D., and J. Krall (2013), Modeling the plasmasphere with SAMI3, *Geophys. Res. Lett.*, 40, 6–10, doi:10.1029/2012GL054300.
- Huba, J. D., G. Joyce, and J. A. Fedder (2000a), The formation of an electron hole in the topside equatorial ionosphere, *Geophysical Research Letters*, 27(2), 181–184, doi:10.1029/1999GL010735.
- Huba, J. D., G. Joyce, and J. A. Fedder (2000b), SAMI2 (Sami2 is another model of the ionosphere): A new low-latitude ionosphere model, *J. Geophys. Res.*, 105(A10), 23,035–23,053, doi:10.1029/2000JA000035.
- Huba, J. D., G. Joyce, S. Sazykin, R. Wolf, and R. Shapiro (2005), Simulation study of penetration electric fields in the low- to mid-latitude ionosphere, *Geophys. Res. Lett.*, 32, L23101, doi:10.1029/2005GL024162.
- Huba, J. D., J. Krall, and D. Drob (2019), Global ionospheric metal ion transport with SAMI3, *Geophysical Research Letters*, 46, doi:10.1029/2019GL083583.
- Isham, B., C. A. Tepley, M. P. Sulzer, Q. H. Zhou, M. C. Kelley, J. S. Friedman, and S. A. González (2000), Upper atmospheric observations at the arecibo observatory: Examples obtained using new capabilities, *Journal of Geophysical Research: Space Physics*, 105(A8), 18,609–18,637, doi:10.1029/1999JA900315.
- MacLeod, M. (1966), Sporadic E theory. I. collision-geomagnetic equilibrium, *Journal of the Atmospheric Sciences (U.S.) Formerly J. Meteorol.*, 23, doi:10.1175/1520-0469(1966)023<0096:SETICG>2.0.CO;2.
- Mathews, J. (1998), Sporadic E: current views and recent progress, *Journal of Atmospheric and Solar-Terrestrial Physics*, 60(4), 413 – 435, doi:https://doi.org/10.1016/S1364-

6826(97)00043-6.

- Mathews, J., and F. Bekey (1979), Upper atmosphere tides and the vertical motion of ionospheric sporadic layers at Arecibo, *Journal of Geophysical Research: Space Physics*, *84*(A6), 2743–2750, doi:10.1029/JA084iA06p02743.
- Nygrén, T., L. Jalonen, J. Oksman, and T. Turunen (1984), The role of electric field and neutral wind direction in the formation of sporadic E-layers, *Journal of Atmospheric and Terrestrial Physics*, *46*(4), 373 – 381, doi:https://doi.org/10.1016/0021-9169(84)90122-3.
- Pancheva, D., C. Haldoupis, C. E. Meek, A. H. Manson, and N. J. Mitchell (2003), Evidence of a role for modulated atmospheric tides in the dependence of sporadic E layers on planetary waves, *Journal of Geophysical Research: Space Physics*, *108*(A5), doi: 10.1029/2002JA009788.
- Picone, J. M., A. Hedin, D. Drob, and A. Aikin (2002), NRLMSISE-00 empirical model of the atmosphere: Statistical comparisons and scientific issues, *J. Geophys. Res.*, *107*, doi:10.1029/2002JA009430.
- Richmond, A. D., and Y. Kamide (1988), Mapping electrodynamic features of the high-latitude ionosphere from localized observations: Technique, *Journal of Geophysical Research: Space Physics*, *93*(A6), 5741–5759, doi:10.1029/JA093iA06p05741.
- Ridley, A. J., Y. Deng, and G. Tóth (2006), The global ionosphere-thermosphere model, *Journal of Atmospheric and Solar-Terrestrial Physics*, *68*(8), 839–864, doi: https://doi.org/10.1016/j.jastp.2006.01.008.
- Roble, R. G., and E. C. Ridley (1994), A thermosphere-ionosphere-mesosphere-electrodynamics general circulation model (time-GCM): Equinox solar cycle minimum simulations (30–500 km), *Geophysical Research Letters*, *21*(6), 417–420, doi: 10.1029/93GL03391.
- Sulzer, M. P. (1986), A radar technique for high range resolution incoherent scatter autocorrelation function measurements utilizing the full average power of klystron radars, *Radio Science*, *21*(6), 1033–1040, doi:10.1029/RS021i006p01033.
- Whitehead, J. (1961), The formation of the sporadic-E layer in the temperate zones, *Journal of Atmospheric and Terrestrial Physics*, *20*(1), 49 – 58, doi: https://doi.org/10.1016/0021-9169(61)90097-6.
- Young, J. M., C. Y. Johnson, and J. C. Holmes (1967), Positive ion composition of a temperate-latitude sporadic E layer as observed during a rocket flight, *Journal of Geophysical Research (1896-1977)*, *72*(5), 1473–1479, doi:10.1029/JZ072i005p01473.

Figure 1.

Arecibo - ion line backscatter power

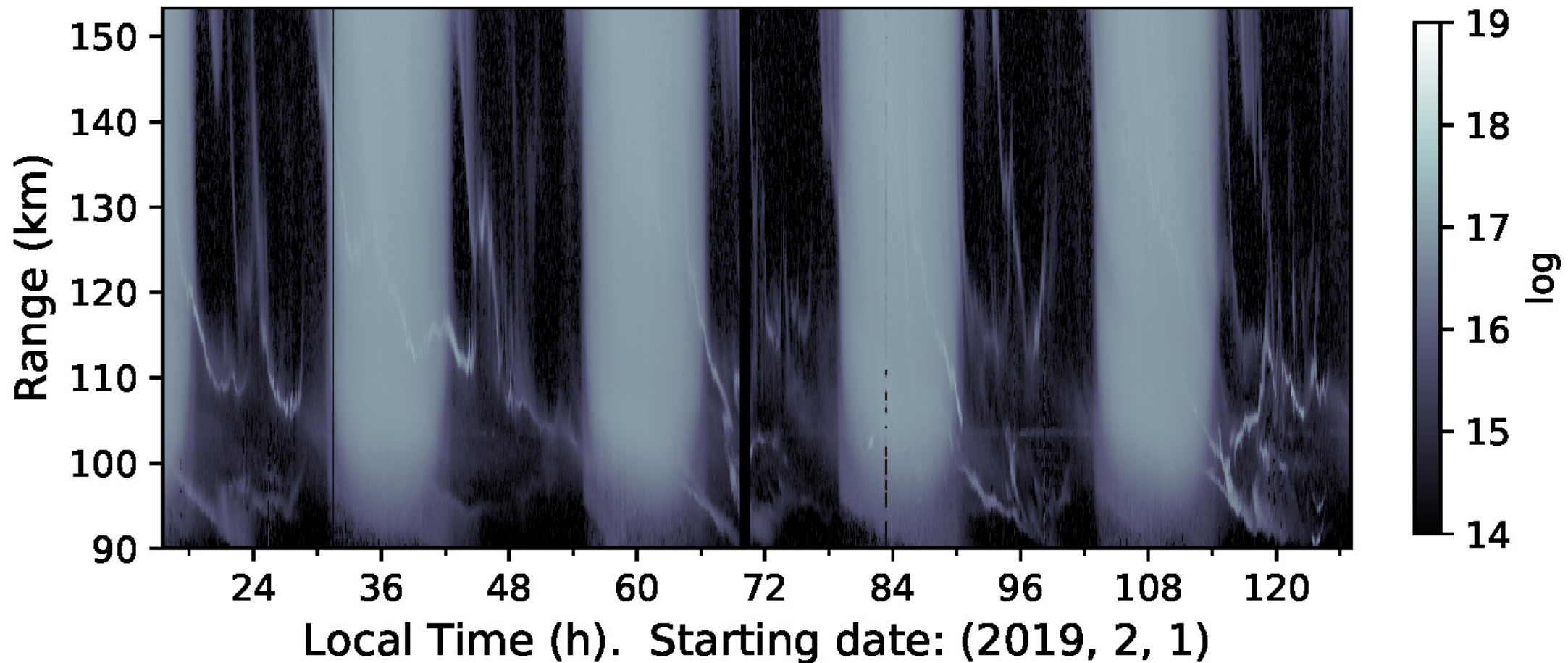


Figure 2.

Arecibo - Edge detection filter - ion line power

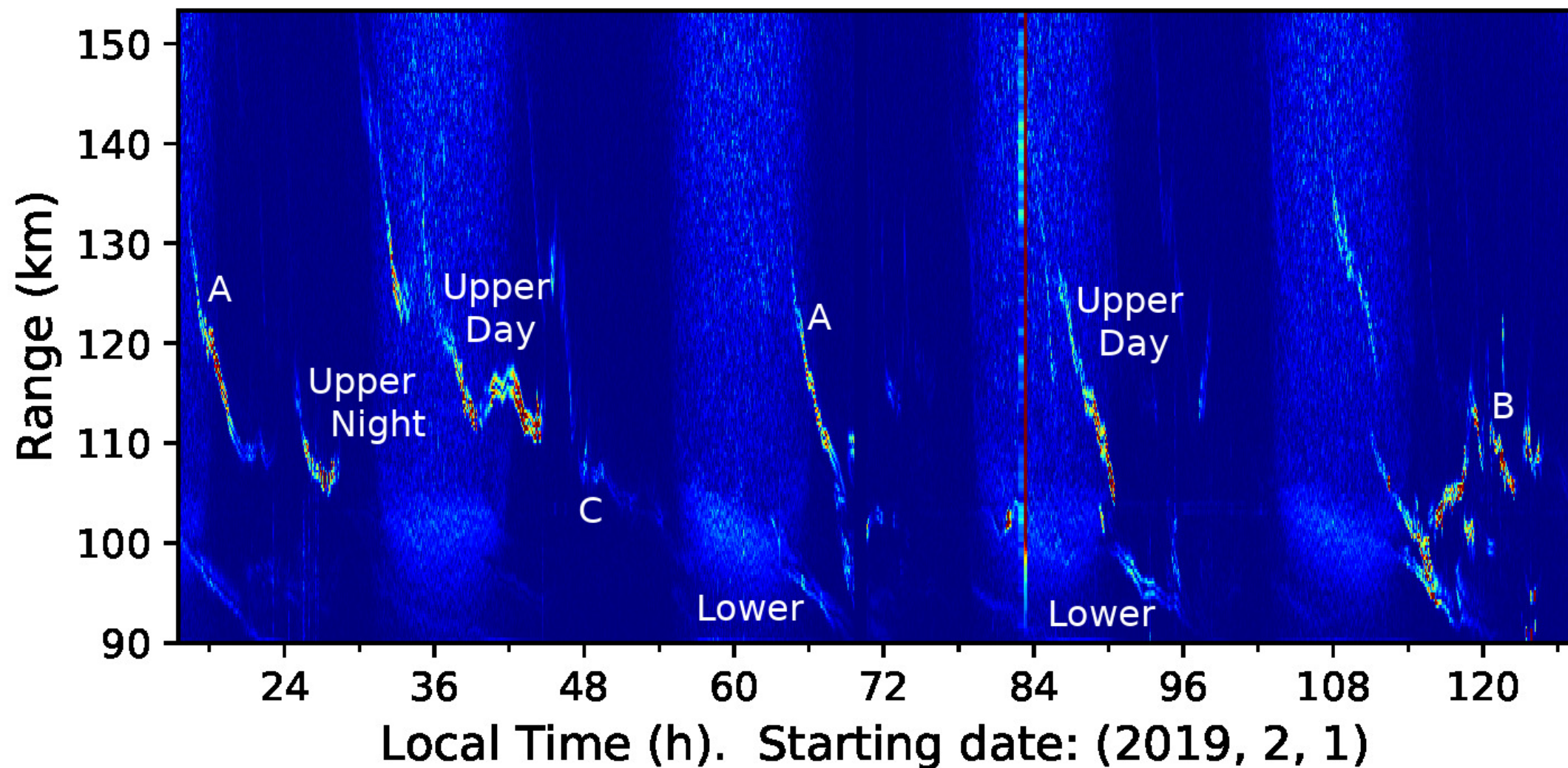


Figure 3.

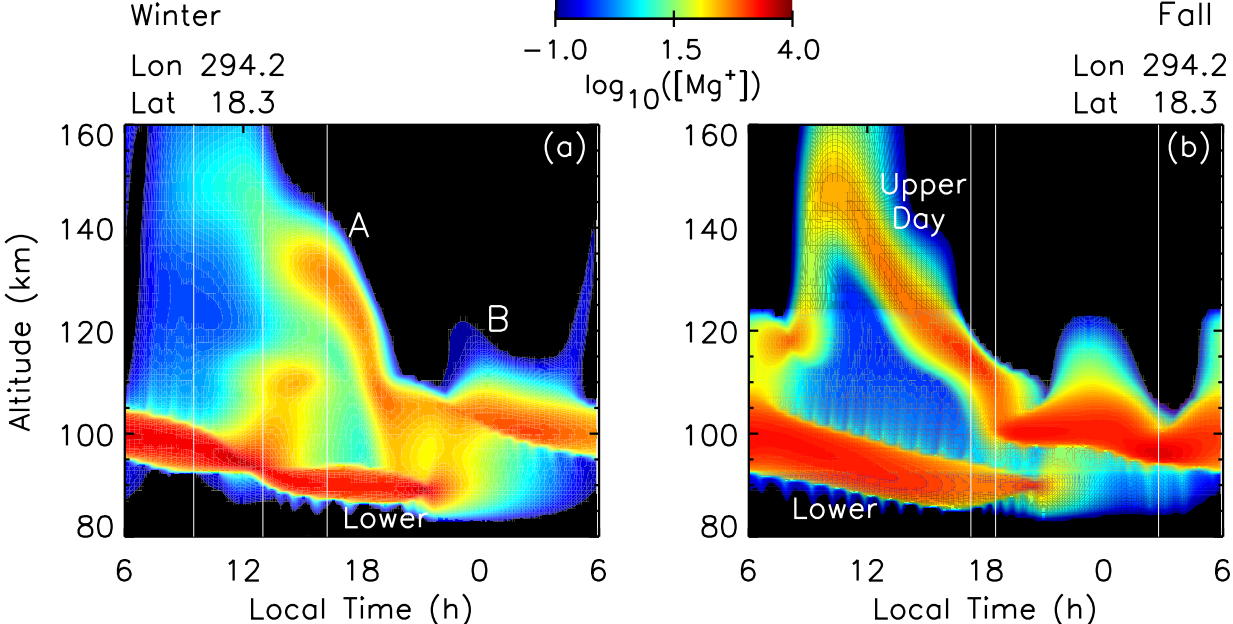
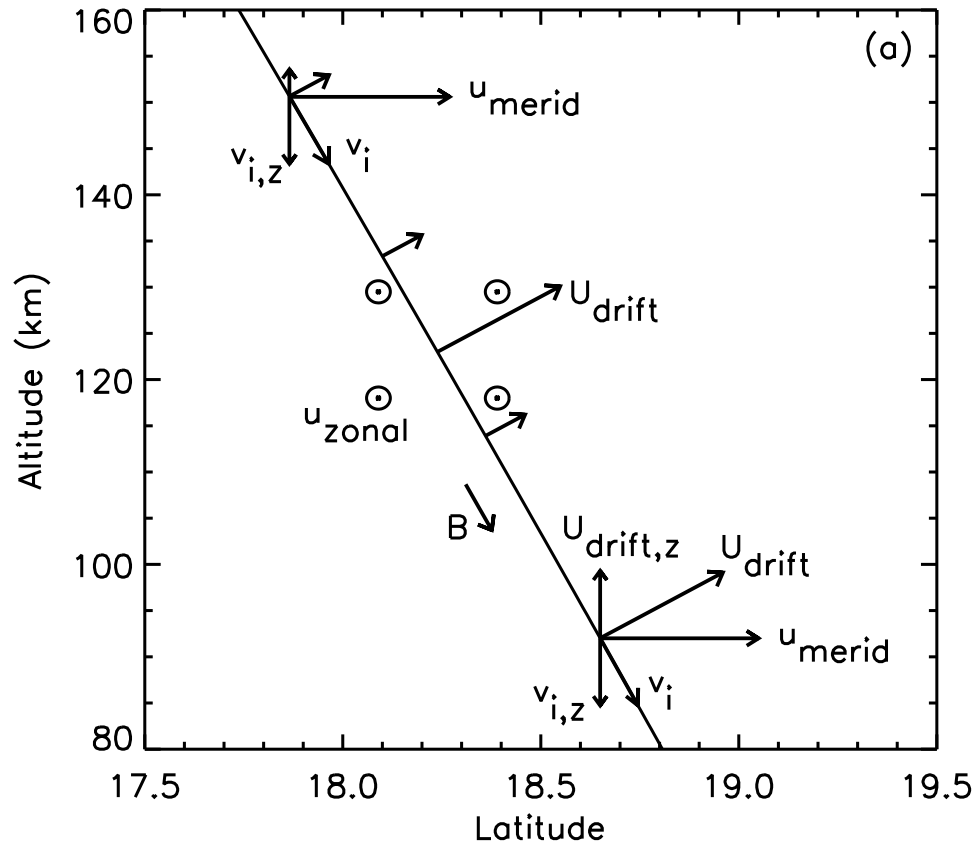


Figure 4.

Lon 294.2
Lat 18.3



UT 17:22
LT 12:59

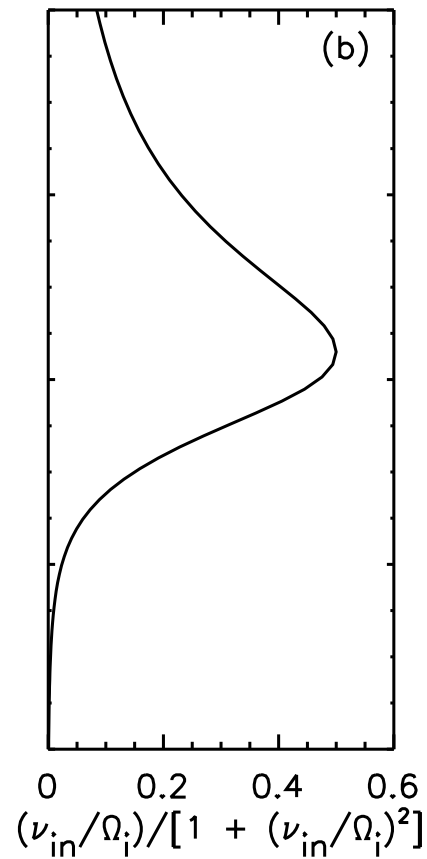
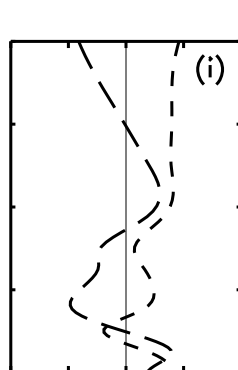
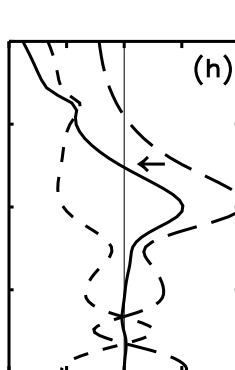
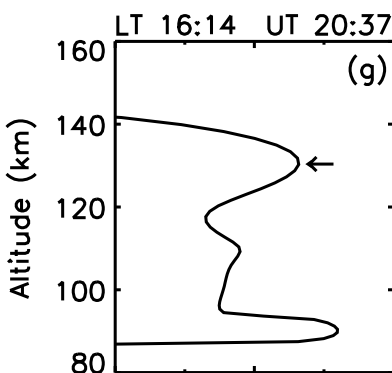
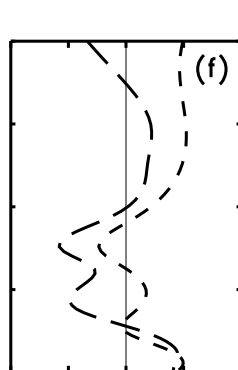
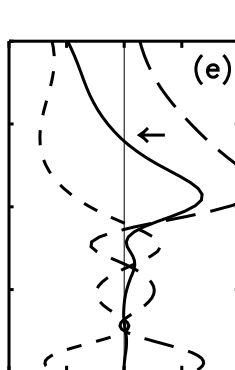
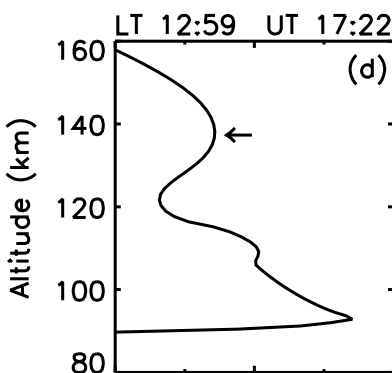
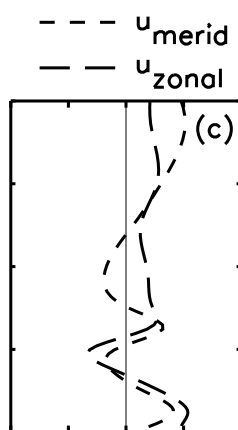
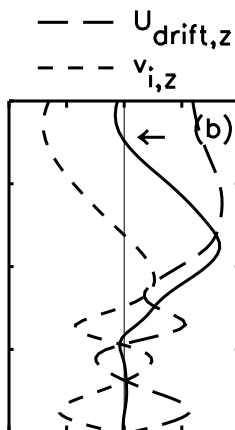
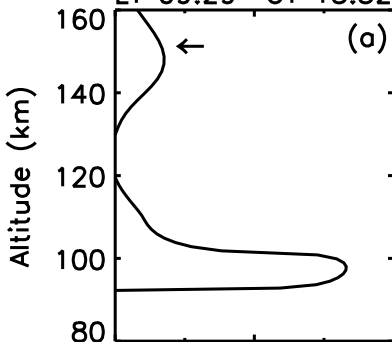


Figure 5.

Winter

Lon 294.2 Lat 18.3

LT 09:29 UT 13:52



1 100 10000 $[Mg^+]$ (cm⁻³)

-10 0 10 20 v_z (m/s)

-30 0 30 60 u_{wind} (m/s)

— $U_{drift,z}$
- - - $v_{i,z}$

- - - u_{merid}
— u_{zonal}

Figure 6.

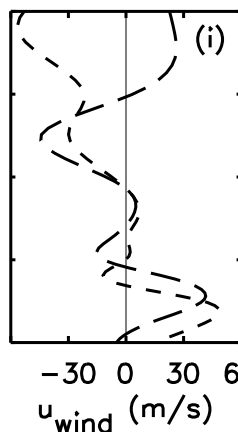
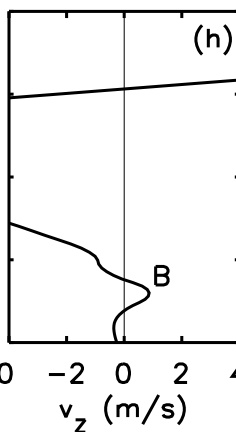
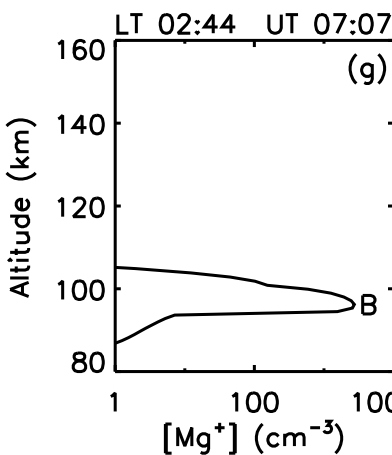
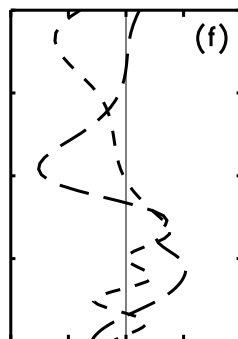
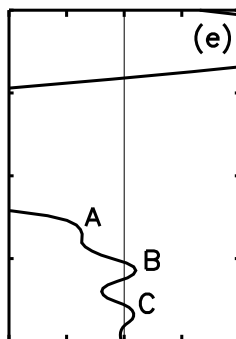
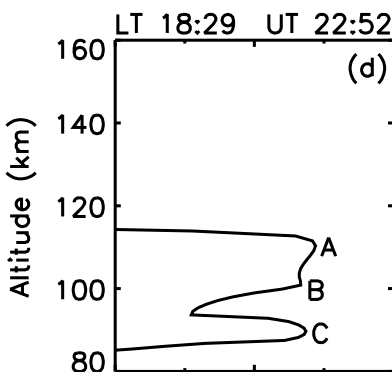
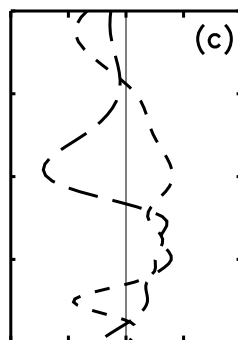
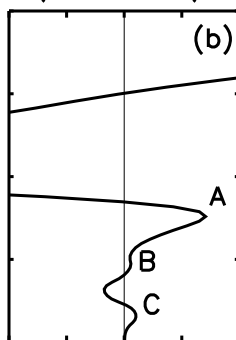
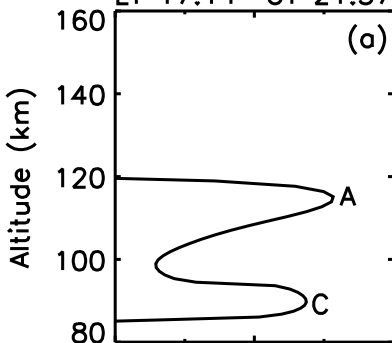
Fall

Lon 294.2 Lat 18.3

LT 17:14 UT 21:37

$v_{i,z} + U_{\text{drift},z}$

--- u_{merid}
 --- u_{zonal}



v_z (m/s)

u_{wind} (m/s)

Figure 7.

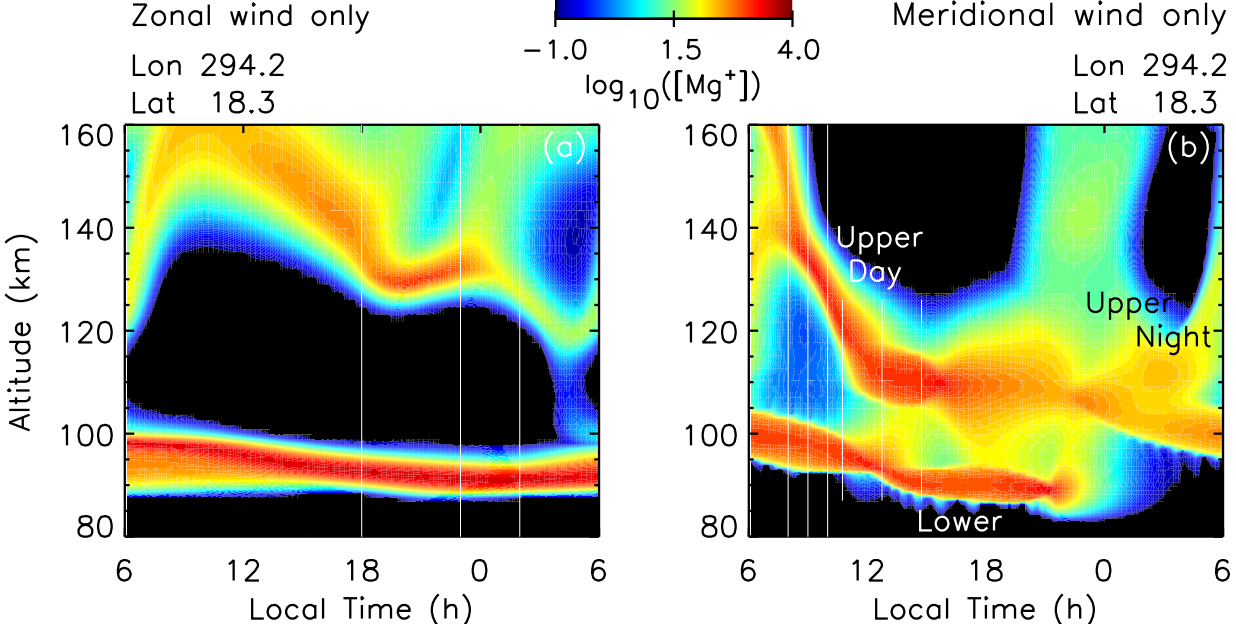


Figure 8.

Zonal wind only

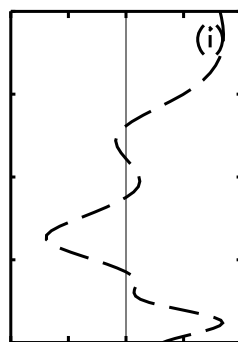
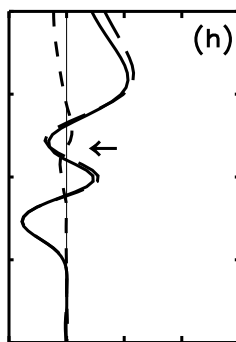
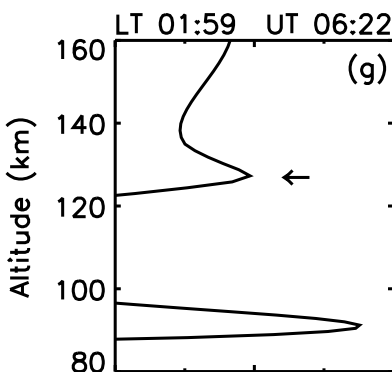
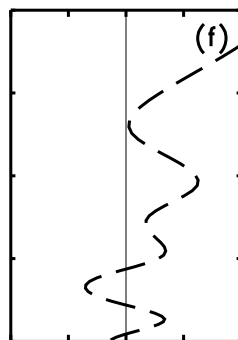
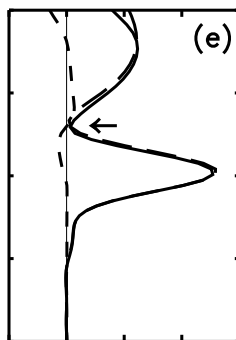
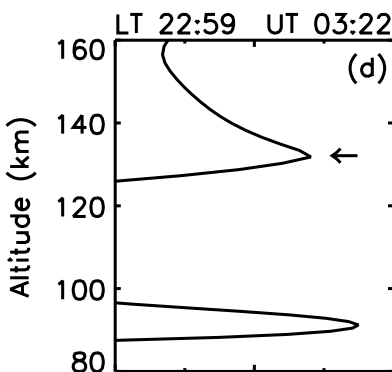
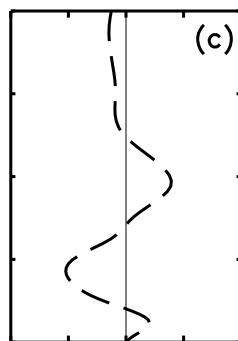
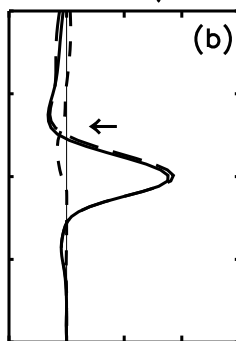
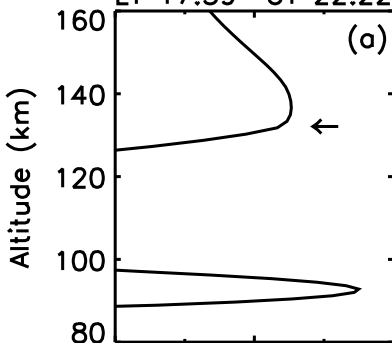
Lon 294.2 Lat 18.3

LT 17:59 UT 22:22

— — $U_{\text{drift},z}$

- - - $v_{i,z}$

- - - u_{zonal}



1 100 10000
[Mg⁺] (cm⁻³)

0 5 10 15
 v_z (m/s)

-30 0 30 60
 u_{wind} (m/s)

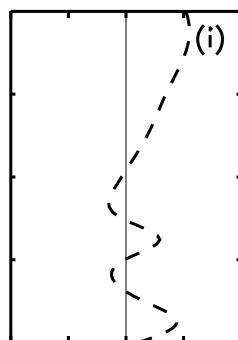
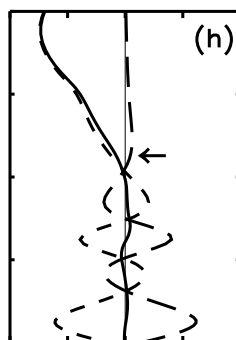
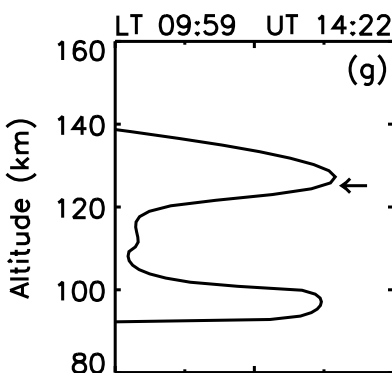
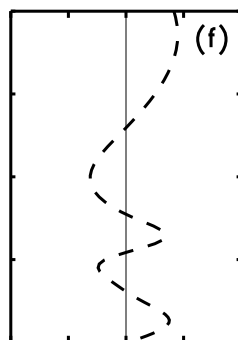
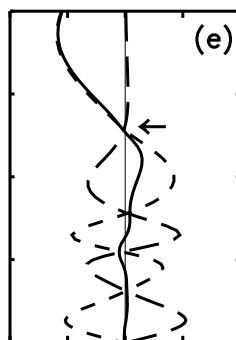
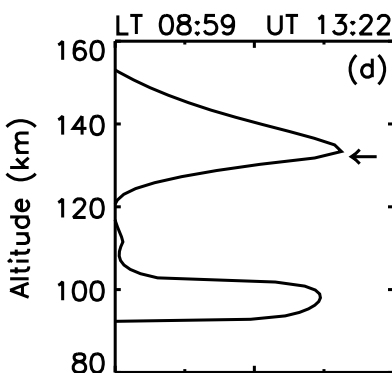
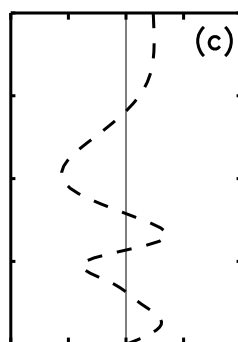
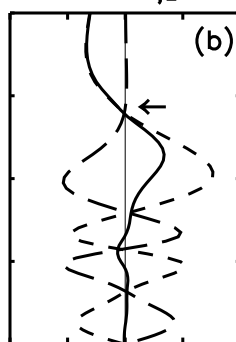
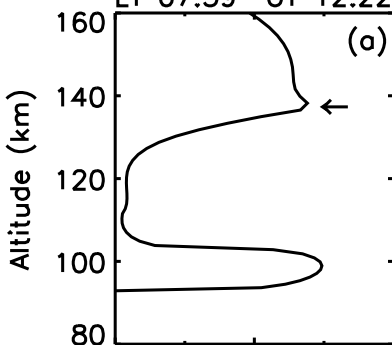
Figure 9.

Meridional wind only
 Lon 294.2 Lat 18.3

LT 07:59 UT 12:22

— $U_{\text{drift},z}$
 - - - $v_{i,z}$

- - - u_{merid}



1 100 10000 $[\text{Mg}^+]$ (cm^{-3})

v_z (m/s)

u_{wind} (m/s)

Figure 10.

Meridional wind only
 Lon 294.2 Lat 18.3

